UV-assisted Robotic Arm Freeforming of SiOC Ceramics from a Preceramic Polymer

Kai Huang[a,*], Anna De Marzi[a], Giorgia Franchin[a], Paolo Colombo[a, b]

[a]Department of Industrial Engineering, University of Padova, Padova 35131, Italy

[b]Department of Materials Science and Engineering, The Pennsylvania State University, State College, PA 16801, USA

* Corresponding author

Abstract

Material extrusion is a very common and facile additive manufacturing technique for ceramic materials, allowing for rapid design and fabrication of 3D structures without expensive tools. However, fabricating sophisticated structures with large spanning parts and overhanging features using this technology is still a challenge. Here, UV-assisted additive manufacturing is enabled by performing material extrusion with the assistance of UV light using mixture of a preceramic polymer and a photopolymer. The rheological properties of the ink were investigated under UV light radiation to optimize the printing parameters to achieve excellent printability. Complex ceramic structures were fabricated with this method, such as spiral and truss structures, which would be very difficult to obtain using traditional material extrusion without sacrificial supports. These structures have potential application in lightweight ceramic components, such as sandwich structures.

Keywords: UV-assisted, freeforming, material extrusion, preceramic polymers, SiOC

1. Introduction

The rise of additive manufacturing (AM) has led to significant developments in the production of advanced ceramic structures, in particular that would otherwise be unattainable via conventional techniques due to prolonged processing times and substantial energy usage. This is related also to the intrinsic hardness and brittleness of ceramic materials[1-3]. The application of digital design coupled with AM technologies has generated new prospects for manufacturing high-performance ceramic components possessing intricate multifunctional architectures, a critical demand in numerous domains, such as aerospace[4-6], energy storage[7-10], environmental conservation[11-14], and biomedicine[15-18]. In recent times, diverse AM methodologies have evolved for ceramic manufacturing, encompassing vat photopolymerization (e.g., stereolithography apparatus (SLA), digital light processing (DLP), and two-photon polymerization (TPP)), material extrusion (e.g., fused deposition modeling (FDM), direct ink writing (DIW), or robocasting (RC)), and binder jetting (BJ)[19-22]. Among these, DIW is a straightforward and versatile technique, adaptable to various materials, exhibiting a high degree of flexibility towards feedstock properties and subsequent sintering processes when compared to alternative AM approaches. This method relies on the viscosity modulation of inks extruded through a nozzle, which must enable both effortless extrusion and post-extrusion shape preservation, characteristic of fluids with shear-thinning behavior coupled with a

sufficient yield stress (Herschel-Bulkley fluids with n<1)[23]. The simplicity and adaptability of DIW have allowed for the manufacturing of different ceramic components using inks containing ceramic powders like Al_2O_3, SiC, SiO_2, TiO_2, Si_3N_4, finding use in an array of applications, ranging from microwave optics to cell growth[24-28]. Nevertheless, finding an appropriate equilibrium between high ceramic powder content and ease of extrusion of the ink, coupled with superior resolution remains a significant challenge. An alternative approach considers the use of preceramic polymer solutions, taking advantage of the solubility of numerous preceramic polymers in various solvents[29]. Employing a liquid feedstock based on preceramic polymers helps avoiding nozzle clogging during extrusion, enabling increased resolution through the application of finer nozzles, some with diameters below 100 μm[30].

With increasing requirements for the micro/macro structure and functionalities of printed components, DIW has been further assisted by various physical stimuli (magnetic, electric, acoustic, thermal, and light) to achieve more advanced and versatile manufacturing processes. For instance, Kim et al. employed a magnetic field to print shape-programmable soft materials responsive to stimuli[31]. Kokkinis et al. used a magnetic field for multi-material DIW, fabricating heterogeneous composites possessing controllable microstructural features and stimulus-responsive soft devices[32]. The introduction of an electric field, achieved through the incorporation of an electrode within the printhead, facilitated the rapid printing of finer filaments on uneven surfaces [33]. Begley et al. conducted a comprehensive exploration of acoustic-

assisted DIW, showing that it is possible to affect the microstructure of colloids [34-36]. Beyond microstructural control using the aforementioned methodologies, the macroscopic structure of printed components was manipulated also through the introduction of thermal and light fields. A thermal field was coupled with DIW to enable rapid ink solidification through the initiation of frontal polymerization, opening the door to the manufacturing of macrostructures[37-39]. Similarly, UV-assisted DIW has been widely used for the fabrication of complex architectures utilizing a range of materials, including polymers [40-42], metals[43], glass[44], and ceramic powders[45]. Generally, UV-assisted DIW follows one of two approaches, depending on the sequence of extrusion and curing steps[46]. In the first approach, UV curing takes place after extrusion, decoupling both steps to ensure robust layer bonding and allowing for the fabrication of gradient functional materials[47]. In the second approach, UV curing occurs simultaneously with extrusion, enabling on-the-fly printing, a method adopted in most investigations due to its numerous advantages: (1) UV light allows for the printing of materials with diverse viscosities, including low-viscosity inks, owing to rapid curing, and (2) in-situ curing permits the creation of structures without supports, facilitating the swift retention of printed shapes and expanding the attainable structural and geometrical complexity. For instance, Maeng et al. succeeded in manufacturing calcium phosphate hierarchical porous scaffolds using a porogen, demonstrating the feasibility of producing freestanding ceramic structures[48].

Previously, only few works had been published concerning the DIW of a preceramic polymer with the assistance of UV radiation. Clarkson et al. employed UV-

DIW strategy to print 3D structures using polycarbosilane with addition of 50 wt% Si_3N_4 powder, although the structures demonstrated could be printable with conventional DIW after viscosity optimization of the feedstock. Wei et al. demonstrated the feasibility of manufacturing log-pile SiOC scaffolds with substantial spanning features using a modified, photocurable silicone resin[49]. However, it is important to note that the rheological properties of their feedstock, even without light irradiation, were already suitable for the fabrication of the proposed structures and, as such, the full potential of UV-DIW was left unrealized.

In this study, we present an efficient and straightforward UV-DIW approach for the fabrication of free-form ceramic structures employing a preceramic polymer. This innovation was made possible by coupling the UV-assisted DIW printing head with a robotic arm, facilitating the swift and facile production of sandwich panels with truss-based cores. Although prior researches on robotic arm assisted printing have already been reported, most of them focus on polymers or metals[50-52], with only few reporting ceramic parts with larger over-hanging and spanning features[48]. In addition, camphene was introduced in the ink composition to create transient pores enabling the release of the gas generated during pyrolysis, leading to crack-free free-formed structures. In this way the photopolymer content could be increased to enable rapid in-situ curing to obtain enhanced printing accuracy. This novel approach broadens the possibilities for manufacturing complex ceramic components, with the provided examples serving as a proof for the production of structural ceramic elements characterized by high rigidity and low weight, thereby holding the potential for

application in aerospace and other advanced sectors.

2. Materials and methods

2.1. Ink preparation

A commercial silicone resin with high ceramic yield, SILRES@H44 (Wacker-Chemie GmbH, München, Germany) was used as preceramic polymer. Pentaerythritol tetraacrylate (PETTA, Sigma Aldrich) was chosen as the photopolymer enabling the curing during printing. A photoinitiator (Irgacure 819, Ciba Specialty Chemicals, Switzerland) was also added to trigger photopolymerization. GF91 (Wacker-Chemie GmbH, München, Germany) was used as crosslinking agent, and camphene (Canfora Naturale Polvere, Rome, Italy) as pore generator for avoiding cracking during pyrolysis. Fumed silica powder (Aerosil R106, Evonik Industries AG, Germany) was used to surround the samples during firing, to avoid the shape distortion. The ink was prepared by dissolving H44 in PETTA with a weight ratio of 2:1, which was determined to be the best formulation in preliminary work (not reported here for the sake of brevity). In fact, a higher amount of H44 leads to poor curing behavior and more PETTA results in low ceramic yield and cracking issues. Then, 1.2 wt% photoinitiator (with respect to total weight) and 8 wt% camphene was added into inks and mixed for 10 mins at 2000 rpm in planetary mixer (ARE 250, Thinky, Japan) at room temperature. 1 wt% of GF91 was also added and mixed for 5 mins. Degassing was performed inside the mixer for 5 mins at 2000 rpm, after transferring the ink into a syringe. The ink composition is reported in **Tab. S1**.

2.2. Free-forming with UV-assisted DIW and pyrolysis

As shown in **Fig. 1**, a robotic arm (Industrial Robot RV-4FR-D, Mitsubishi electric, Japan) was used to perform the free-forming of structures, because of its high degree of freedom of movement provided by its 6-axis articulation. A syringe containing the ink was connected to a screw extruder into which the ink was fed by compressed air (at 0.5 Bar). Then, the extruder was installed on the robotic arm and its movement as controlled by a home-made program based on Matlab (MathWorks, USA), together with the switching on and off of the UV LEDs, which were set to on during extrusion and to off during nozzle traveling (more details about the printing setup can be found in our previous paper[44]). Printing was performed using a UV-shielded nozzle with a diameter of 0.58 mm, with a printing speed of 0.2 to 1.6 mm/s. The UV setup was added to the printhead as shown in previous literature[44]. Briefly, the UV setup is composed of an array of UV-LED chips around the nozzle (Vieweg GmbH, Germany). The intensity is around 98 mW/cm^2 at outlet point of nozzle measured by a power meter (PM400, Thorlabs Inc., USA), and they operate at a wavelength of 395 nm. After printing, the samples were placed into tube furnace for pyrolysis in N_2 atmosphere with the following heating program: from room temperature to 460°C with heating rate of 1°C/min and dwelling for 1h to decompose the PETTA; then, increasing to 1000°C with heating rate of 2°C /min and dwelling for 1h to complete ceramization. To mitigate the deformation during pyrolysis, particularly for structures with overhanging features such as triple helix and twisted basket, the samples were submerged into fumed silica powder. The lightweight and fluffy powder facilitated shape retention while permitting

shrinkage. After pyrolysis, the samples were transferred into water and underwent ultrasonic cleaning for 15 mins to eliminate silica residues on the surface. The chemical structure evolution from the polymerization to pyrolysis into SiOC amorphous network is illustrated in **Fig. 1**.

2.3. Characterization

The rheological properties of the ink were measured by a rotational rheometer (Kinexus lab+, Netzsch, Germany) equipped with a 50 mm diameter plate-plate geometry at room temperature, with a gap of 0.29 mm. The flow curves were measured with shear rate interval from 0.01 to 100 s^{-1}, and the frequency 1 Hz. The shear strain interval for amplitude sweep was 0.001 to 100 %. An amplitude sweep as a function of time under UV light was performed using a transparent plate with a UV lamp (OmniCure 2000, Excelitas Technologies Corp., USA) underneath. The intensity of the UV lamp was set to be the same as that of the UV setup, to simulate the rheological behavior during printing. X-ray diffraction (XRD, AXS D8 Advance, Bruker,Germany) was employed to investigate the crystalline phase assemblage on powders obtained by grinding pyrolyzed samples. Thermo-gravimetric (TG) analysis (STA409, Netzsch, Germany) was carried out in N_2 atmosphere from room temperature to 1000℃ with a heating rate of 5℃/min.

Fourier-transform infrared spectrometry (FTIR, Is10, Nicolet, Thermo Scientific, USA) was used to investigate the conversion rate of vinyl groups of the ink under different UV irradiation times. The curing depth was investigated by measuring the thickness of the cured part under different irradiation doses using a digital caliper. In

these tests, the same UV intensity at different irradiation times was provided by the same UV lamp used in the assessment of rheology.

The size of samples before and after pyrolysis was measured by a digital caliper. Four-point bending tests were carried out by a universal testing machine (Instron 1121 UTM, Instron Danvers, MA, USA), where the loading span was 1/3 of the support span and the crosshead displacement rate was 0.5 mm/min. Samples with a dimension of 38×11×9 mm^3 were tested with a span length of 27 mm.

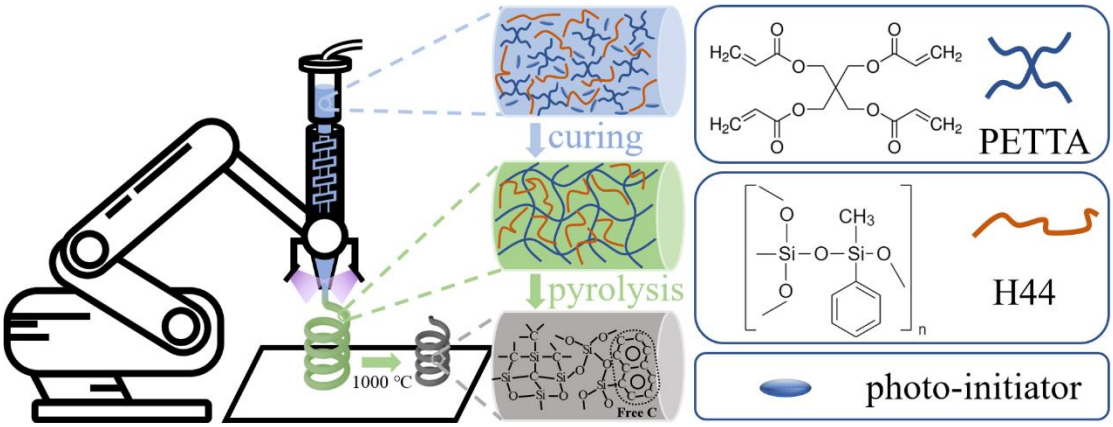

Fig. 1. Schematic illustration of free-forming printing with combination of DIW and UV curing, and structure evolution of the ink during curing and pyrolysis.

3. Results and discussion

3.1. Rheological properties of the ink with/without UV light

Rheological properties play an important role in extrusion-based 3D printing since a shear thinning behavior, yielding under high shear stress and a high storage modulus are required for smooth extrusion and shape retention. **Fig. 2a** shows the flow curves

of the ink without UV light, showing a relatively low viscosity of 165 Pa·s. Differing from typical printable inks for DIW, the viscosity of our ink was nearly constant in the testing shear rate range, indicating no thixotropic shear thinning behavior. Furthermore, a linear relationship between shear stress and shear strain (see **Fig. 2b**) shows it possesses the characteristics of a Newtonian fluid. As shown in **Fig. 2c**, the loss modulus (G″) was consistently higher than the storage modulus (G′) and no yielding point could be observed, demonstrating a poor ability to maintain printed shape. Therefore, it's obviously impossible to print this ink by traditional DIW. However, the assistance of UV light enabled successful printing due to fast in-situ curing. To investigate the influence of UV irradiation on the change of rheological properties, the modulus was measured as the function of time, and the UV light was switched on at 30 s and kept on for further 70 s until the modulus reached a plateau. As shown in **Fig. 3**, the shear modulus increased very rapidly by several orders of magnitude after the UV light was switched on, up to ~10^7-10^8 Pa, which is high enough to provide self-supporting. The gelling time was 10.6 s, determined by the crossing point of G′ and G″. Although it seems that the gelling time was longer than what would be required for in-situ curing and self-supporting, it is not actually necessary to completely cure the ink in order to enable maintaining the printed shape. In fact, the immediate curing of the surface of the extruded filament at the beginning would help to provide most of the self-supporting, and the printing speed could also be optimized to couple with the degree of curing, as proved by the successfully printed samples (see **Figs. 7**, **9**).

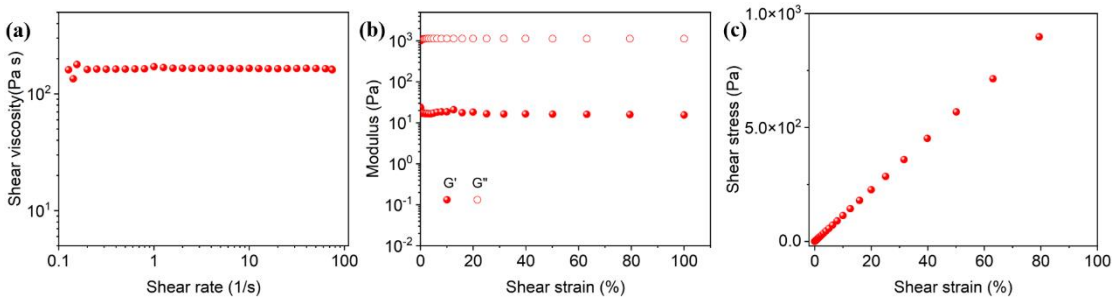

Fig. 2. Rheological properties of the ink without UV light: (a) shear viscosity as function of shear rate; (b) shear stress vs shear strain; (c) storage and loss modulus vs shear strain.

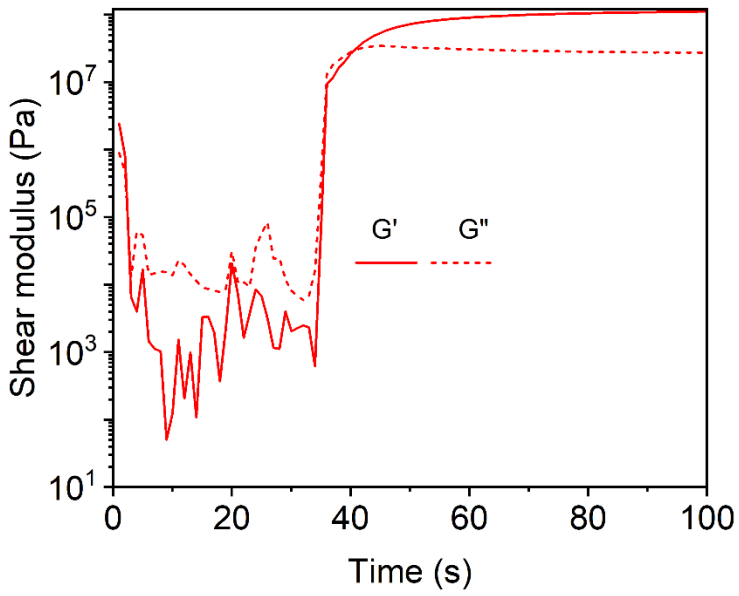

Fig. 3. Shear modulus as a function of time under UV irradiation (UV light was switched on at 30 s).

3.2. Curing behavior

To better understand the curing process, the curing degree as a function of

irradiation time was investigated using FTIR, where the change in the absorption peaks is related to the degree of polymerization. As shown in **Fig. 4**, characteristic peaks of H44 were located at 460-520 cm^{-1} (Si-O-Si rocking vibration), 700 and 730 cm^{-1} (CH_3-Si-Benzene), 900-1250 cm^{-1} (Si-O-Si stretching vibration), 1270 cm^{-1} (symmetric deformation of $–CH_3$ in $Si-CH_3$ configuration); characteristic peaks of PETTA were located at 1600-1645 cm^{-1} (C=C stretching vibration), 1730 cm^{-1} (C=O stretching vibration) , 2995-3095 cm^{-1} (C-H stretching vibration of $-CH=CH_2$ group)[45,53-55]. The UV curing reaction, specifically addition reaction of C=C bonds in this case, is initiated by free radicals generated through the dissociation of the photoinitiator upon exposure to UV light. Therefore, the quantity of C=C bonds is indicative of the degree of cross-linking, as manifested by the intensity of peaks in the FTIR spectra. We can observe that the C=C peaks gradually decreased with the increasing of UV irradiation time, indicating the progression of the cross-linking caused by radical polymerization. Relative Band Ratio Method was adopted to quantify the curing degree by calculating the relative intensity of the FTIR peak attributed to C=C stretching (1600-1645 cm^{-1}) for both UV-exposed and non-UV-exposed samples, with the FTIR peaks attributed to C=O stretching absorption (1671-1805 cm^{-1}) as inner standard peak, since it is unchanged during the reaction[56]. The conversion rate C=C bond $\boldsymbol{\alpha}$ determined by the irradiation time $\boldsymbol{t}$ was calculated as following:

$$\boldsymbol{\alpha}\,(t) = \left(1 - \frac{A^0_{C=C}/A^0_{C=O}}{A^t_{C=C}/A^t_{C=O}}\right) \times 100\% \quad (1)$$

where $A^0_{C=C}/A^0_{C=O}$ is the integral area of the C=C/C=O peak before irradiation with UV light, $A^t_{C=C}/A^t_{C=O}$ is the integral area at irradiation time $\boldsymbol{t}$. The values of the

integral areas are listed in **Tab. S2**.

The conversion rate of the double carbon bond is reported in **Fig. 5a**, showing that it increased very fast at the beginning, then taking ~10-15s to reach a plateau, which corresponds to the gelling point mentioned above. The behavior can be attributed to the inhibition of the monomer mobility by the newly formed chains after the gelling point[57,58], leading to a maximum curing degree of 45%. A low curing degree may result from the high content of Silres H44, which is twice the amount of PETTA. Consequently, the polymerization may be hindered by the reduced probability of PETTA molecules of encountering each other. Additionally, the introduction of the cross-linking agent GF91 will accelerate the cross-link of H44 even at room temperature (although at a very low rate) to further block the chain propagation. However, we should point out that freeforming printing is achieved in this manner even with low curing degree, as indicated by the well-printed, complex structures produced.

In addition, the penetration depth and critical energy dose for starting the polymerization were measured under a UV intensity of 98 mW/cm^2, and quantified according to Jacobs' equation[59-61]:

$$C_d = D_p \cdot ln\left(\frac{E}{E_c}\right) \quad (2)$$

where C_d is the curing depth, D_p is the penetration depth, defined as the value at which the irradiance corresponds to 1/e (e is the base of natural logarithms) of the surface irradiance, E is the energy dose per area, E_c is the critical energy where the curing depth is zero. **Fig. 5b** shows that results of the curing depth are well-fitted by Jacobs' equation, with a high value for R^2 of 0.97. It's worth noting that the penetration

depth was 0.56 mm and only 1.5 s (calculated from the fitting curve at a UV intensity of 98 mW/cm^2) are required to reach the curing depth of 0.58 mm (corresponding to the nozzle diameter) under the printing conditions used in this work, indicating that it is possible to achieve efficient free-forming printing using an appropriate printing speed.

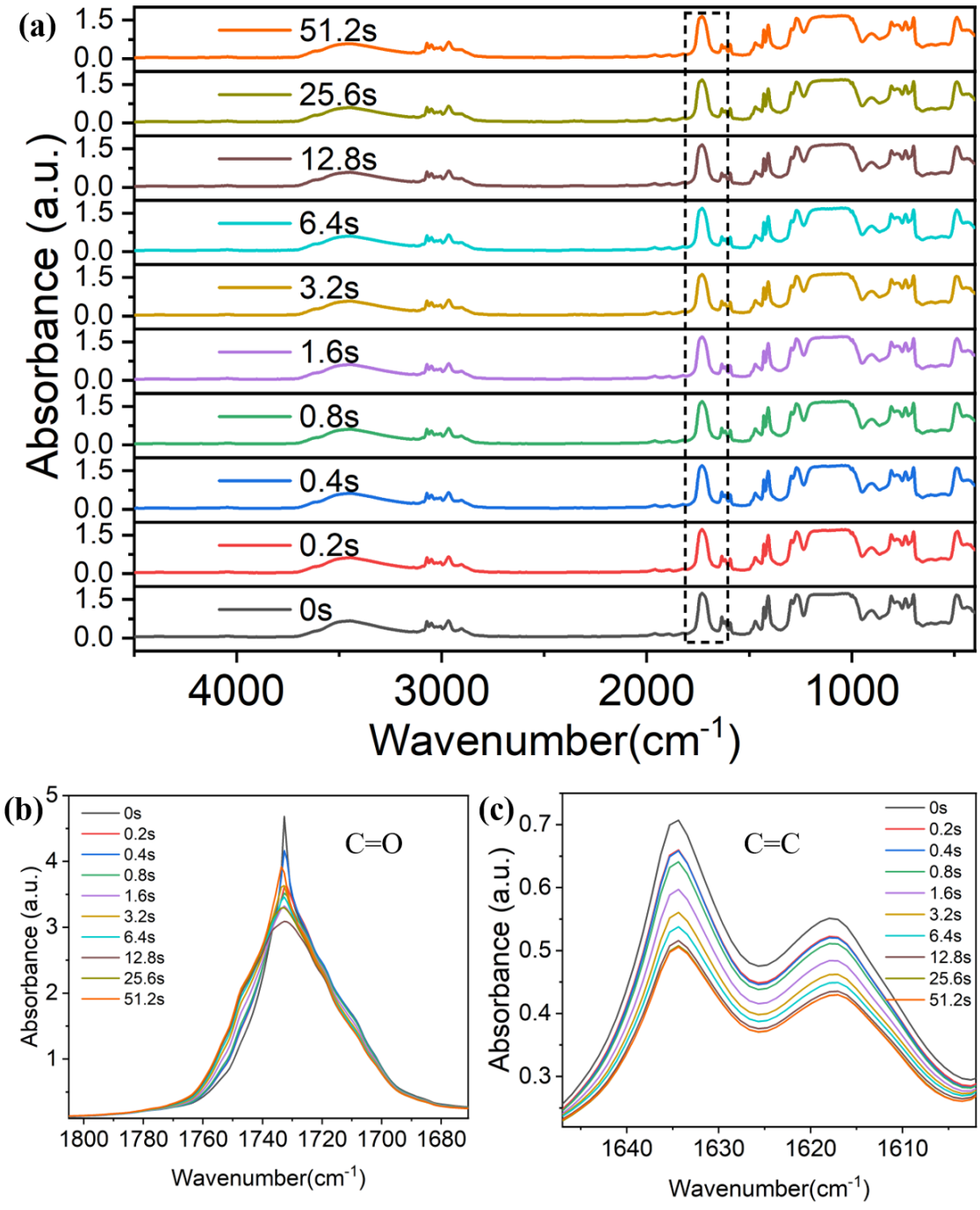

Fig. 4. (a) FTIR spectra for different UV irradiation times from 0 to 51.2 s, and enlarged images of peaks attributed to: (b) C=O and (c) C=C.

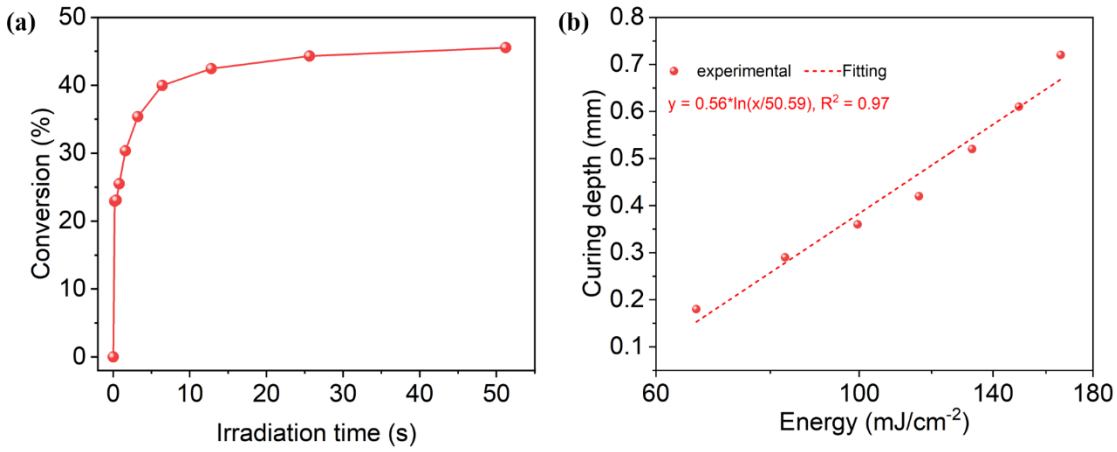

Fig. 5. (a) Curing degree vs irradiation time and (b) curing depth vs UV radiance.

3.3. Self-supporting and free-forming 3D printing

To optimize the printing parameters using the robotic arm, aiming at appropriate printability and self-supporting, we printed several vertical filaments (3 cm long) at different speeds, varying from 0.2 to 1.6 mm/s (see **Fig. 6a**). The flow rate was calibrated to match the extrusion speed with the printing speed, as indicated in **Fig. S1**. We can observe that the filament showed a large deformation when printed at 1.6 mm/s, with the upper part collapsing under its own weight due to the insufficient curing rate. With the decreasing of printing speed, the filament became more straight in the vertical direction, with the best result obtained at 0.4 mm/s. However, clogging occurred due to fast curing near the nozzle tip when the speed was decreased to 0.2 mm/s (not shown in this work). We can conclude that, when the printing speed is faster than the curing

speed ($V_{curing} < V_{printing}$), the curing front increasingly lags behind the nozzle, causing the non-yet-cured deposited filament to collapse and deviate from the designed path. In contrast, if the curing speed is slower than the printing speed ($V_{curing} > V_{printing}$), the curing front gets closer to the nozzle, likely leading to the clogging of the nozzle. Moreover, the filament diameter tends to be close to the nozzle diameter when decreasing the printing speed, which can be explained considering that a low printing speed gives extruded filament more time to be cured in situ, so the filament expansion is limited. Even though the optimized printing speed is low, due to the limitation of our experimental conditions, it could be increased using a more powerful LED setup. **Fig. 6b** shows a 10 cm vertical filament printed at 0.4 mm/s, demonstrating its very well-maintained shape without significant deformation. Likewise, a spiral polyline structure and a 15 mm helix (see **Fig. 6c, d**) were printed with optimized parameters, to demonstrate the suitability of this method to fabricate suspended structures with a high degree of control over structures with sharp angles. Furthermore, filaments with length of 3 mm were printed at tilted angles of 30 and 45° (**Fig. S2a**), showing no sagging even with a high length/diameter ratio of 50. An "A" shape structure and a cantilever were also manufactured to quantify the shape distortion with respect to the spanning and overhanging of the structures. As shown in **Fig. S2b**, the "A" shape structure consisted of filaments of different length (0.5 to 3 cm) with two ends supported; no deformation was detected after printing. The cantilever was printed continuously, and was composed of a 1 mm vertical part and a suspended part with different lengths. No sagging was observed up to 2 cm of the cantilever, while 1 mm sagging occurred at the

end of a 4 cm long filament, leading to a 2° inflection (**Fig. S2c**), which is anyway rather small. Longer overhanging and suspended features would be achieved by increasing the UV intensity and using finer nozzles. In any case, the self-supporting ability of the formulated ink is definitely sufficient to enable the adopted system to achieve free-form printing (see below).

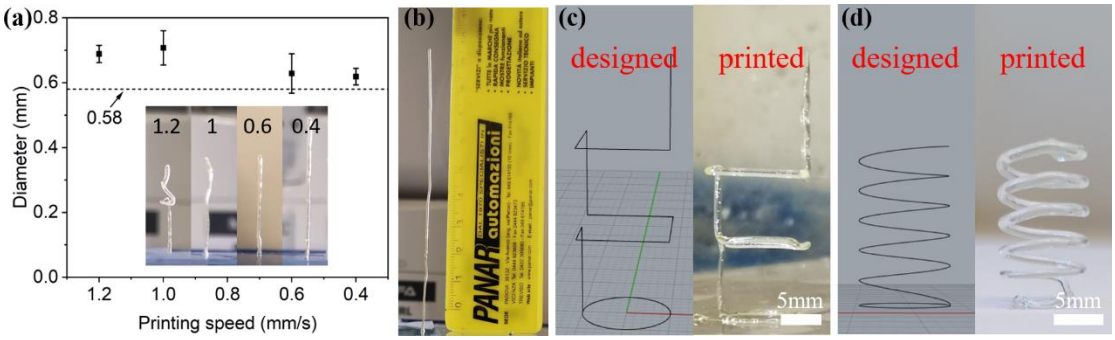

Fig. 6. (a) Vertical filaments printed at different printing speeds; self-supporting structures printed with optimized speed (0.4 mm/s): (b) 10 mm standing vertical filament; (c) spiral polyline structure, and (d) 15 mm helix with 5 pitches.

The advantage of employing a robotic arm is that a higher degree of freedom can be achieved, enabling printing in all directions, when compared with Cartesian or delta printer setups. To demonstrate the suitability of this method for free-form printing of structures not easily achievable using conventional DIW, we fabricated some truss structures that could constitute the core part of a sandwich panel, consisting of polylines printed in a non-continuous way. The various truss structures showed a good retention of the given shape, both before and after pyrolysis (**Fig. 7a, see Movie S1-3 in Supplementary Information**). The base of the structure was composed of

triangle/rectangle on which filaments were deposited tilted at an angle of 60°or 45° to form a triangular/quadrangular pyramid. Moreover, a more complex structure consisting of two triangular pyramids connecting at vertex was printed, featuring spanning filaments linking the vertexes with good connection at the joints. We can observe that the joining at the vertices was not very smooth, because a few seconds stop-by was adopted to ensure achieving a good connection, which resulted in redundant ink extrusion. This would be avoided by increasing the intensity of the LED setup and further optimizing the movement of the robotic arm, in the future. Furthermore, a triple helix (**Fig. 7b**) and a twisted basket structure (**Fig. 7c**) were fabricated by printing a single helix or a straight line in sequence with the tilting/rotating of the nozzle, thanks to the high degree of freedom given by robotic arm (**see Movie S4-5 in Supplementary Information**). In this way, the already printed part was bypassed avoiding a collision with the moving nozzle, which would be very difficult to achieve using a traditional DIW setup without destroying the already printed part. With this approach, free-formed samples were obtained, showing very limited deformation or collapse. No defects like cracks or pores were observed on the surface or in the cross-section of the pyrolyzed filaments (**Fig. S3**), which is attributed to the addition of camphene (samples without camphene possessed defects like cracks and bloating, see **Fig. S4**). Thermal analysis (**Fig. 8**) reveals the evaporation of camphene is completed at 180°C, creating transient pores for the gas release due to the decomposition of PETTA in the 350-520°C temperature range, and the polymer-to-ceramic transformation of H44 occurring at 500-800°C. After that, no significant

weight loss was observed, suggesting that the ceramization was complete, achieving a ceramic yield of 40.1 wt%. XRD analysis of pyrolyzed samples (**Fig. S5**) shows a broad peak, indicating the formation of an amorphous SiOC phase, as expected, without the formation of crystalline phases such as SiC or SiO_2.

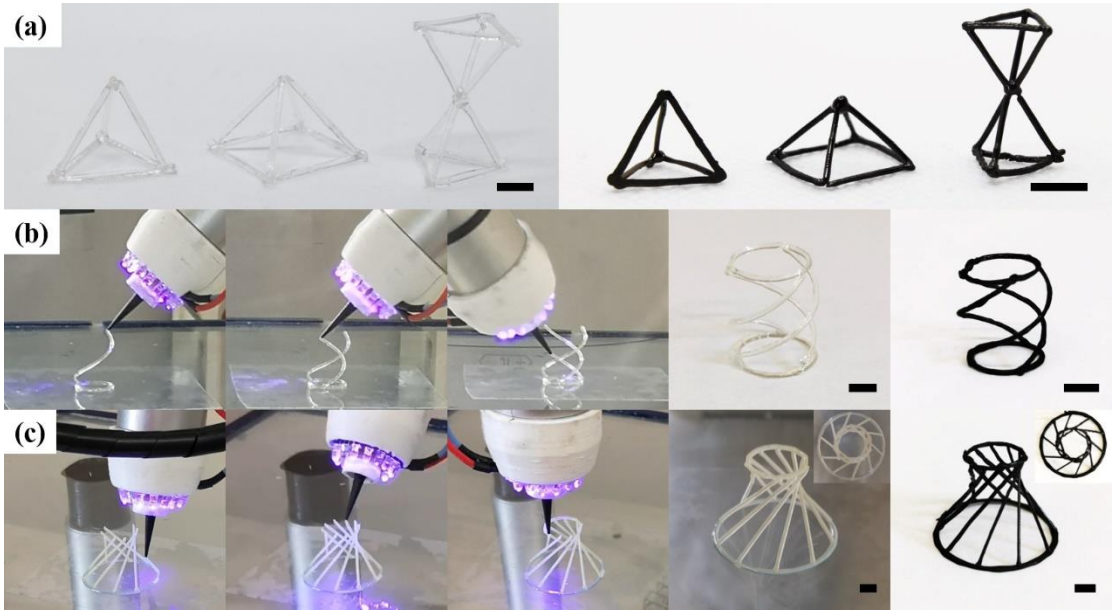

Fig. 7. (a) Various sandwich core structures: triangular and quadrangular pyramid, joined pyramids with spanning features, before and after pyrolysis; printing process of: (b) triple helix structure and (c) twisted basket, as well as printed samples before and after pyrolysis. Scale bars are 5 mm.

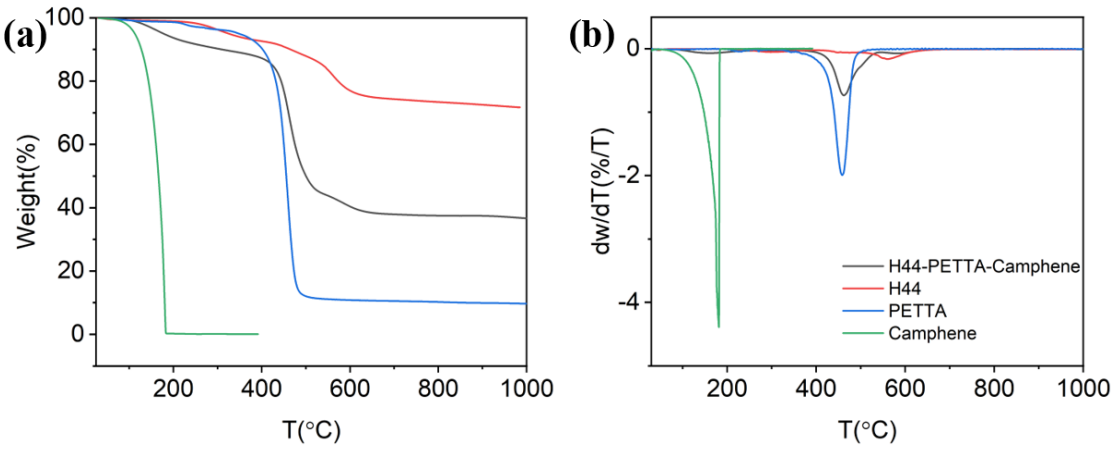

Fig. 8. Thermal analysis: (a) TG and (b) DTG

3.4. Mechanical properties

Considering that ceramics are widely used as structural supporting materials, we fabricated sandwich panels and characterized their mechanical properties, serving as a proof-of-concept for potential applications as lightweight structural ceramic components. As shown in **Fig. 9a (see Movie S6 in Supplementary Information)**, the sandwich panel consisted of faces with parallel filaments on the top and bottom, as well as a core part based on a body-centered cube (BCC) unit. A very good shape retention could be observed after printing with geometry accuracy over 98% when comparing with the original design (**Tab. S3**), and only very limited deformation occurred after pyrolysis. A homogeneous linear shrinkage after pyrolysis was obtained in different directions with an average value of ~21%, leading to a volumetric shrinkage of 50%. No observable cracks or pores were found on the surface and in the cross-section of the filament (**Fig. 9b, c**). The results of the four-point bending test are given in **Fig. 10a**

(failure loads are listed in **Tab. S4)**. During the loading, the sandwich structure experienced a linear elastic deformation followed by some minor failures, attributable to the breaking of joining points in flat face areas, indicated in **Fig. 10a1** and **a2**. Subsequently, the joining point within the core part broke under continuous loading, leading to a major failure (**Fig. 10a3**). Afterwards, progressive failures occurred with the breaking of additional joining points (**Fig. 10b4** and **b5**). Generally, the Weibull distribution function based on weakest link postulate is commonly used for the statistical analysis of the mechanical properties of ceramics, revealing the probability of failure at a given load[62,63]. Here, the two-parameter Weibull cumulative distribution function was adopted according to[64,65]:

$$lnln\left(\frac{1}{1-P_f}\right) = m\ ln\ l_f - m\ ln\ l_0 \quad (3)$$

where P_f is the probability of failure, l_f is the failure load, l_0 is the characteristic failure load, and *m* is the Weibull modulus.

When the number of total specimens $N \leqq 30$, P_f can be calculated by ranking l_f in ascending order using the Benard's approximation for the median ranks[66-69]:

$$P_f = \frac{f-0.3}{N+0.4} \quad (4)$$

According to the formulas (3) and (4), a linear regression fitting was performed on the Weibull distribution of the failure load, with $lnln\left(\frac{1}{1-P_f}\right)$ as a function of $ln\ l_f$ (as shown in **Fig. 10b**). The l_0 and *m* values derived from the fitting were 38.8 N and 6.1, respectively, with a high correlation coefficient of R^2 = 0.98, suggesting that this Weibull distribution function is quite appropriate to describe the failure load of the samples produced in this work. The resulting value of $m \sim 6$ suggests an accelerated

rate of failure and fast wear-out, which is quite common for brittle materials[64]. In addition, the narrow distribution of the failure load indicated by *m* reflects the reliability of results. The failure load value was limited, but the pyrolyzed sandwich panels had a total porosity of about 91.3 ± 1.1 vol% (designed porosity of 94 vol%), which makes them of interest as lightweight structural components.

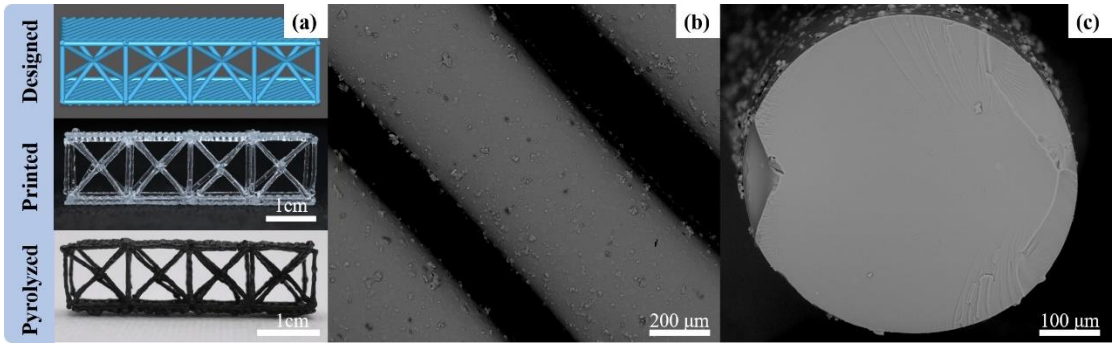

Fig. 9 (a) The designed, printed and pyrolyzed sandwich structure; (b) and (c) SEM image of surface and cross-section of filament.

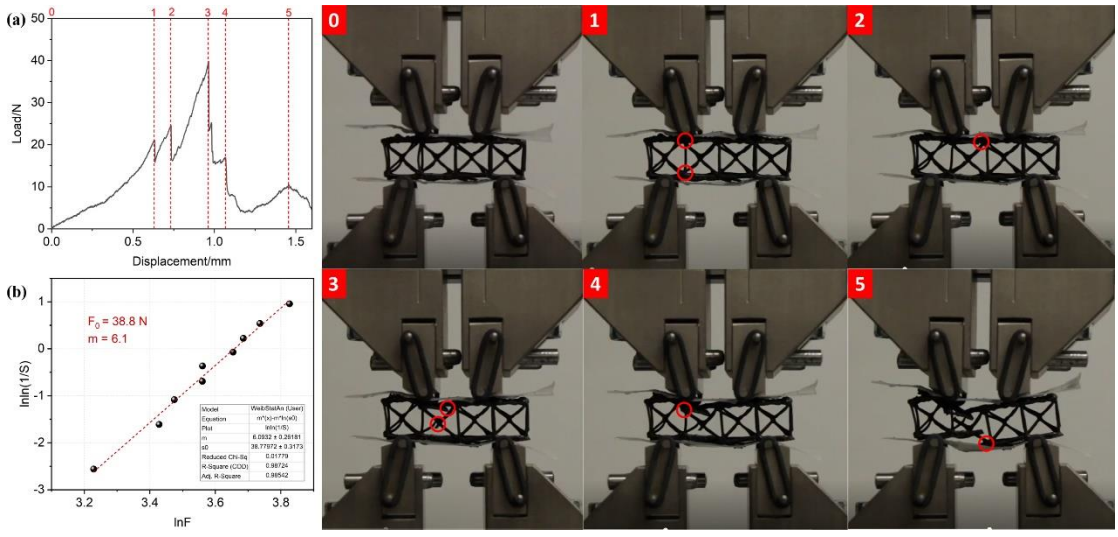

Fig. 10 (a) Representative load-displacement curve and images during flexural test (0-5); (b) Weibull distribution of failure load.

In addition, in order to provide more details on the mechanical properties of the SiOC material obtained from this ink formulation, 0-90° scaffolds with 70 vol% porosity and a size of 10 ×10 × 3 mm^3 were printed and pyrolyzed for comparison with literature data (see **Fig. S6a-c**). Compressive tests showed typical stress-strain curves, with a linear stress-strain response up to the peak stress, followed by progressive failure caused by gradual crushing occurring layer by layer (**Fig. S6d**). Compressive strength value of 4.9 ± 0.5 MPa (70 vol% porosity), comparable to those reported for SiOC structures with similar total porosity (see **Tab. S5**), were achieved using the ink developed in this work, confirming the good quality of the printed structures both before and after pyrolysis.

Conclusions

In this work, a facile and effective free-forming method of ceramic parts from a preceramic polymer and photopolymer was demonstrated, based on a combination of DIW and UV light. UV in situ curing not only makes it possible to print a liquid ink with low viscosity, but also greatly expand the range of printable architectures which otherwise would be difficult to fabricate by DIW without supports. The investigation on the rheological properties of the ink with and without UV light showed a rapid increasing of viscosity and storage modulus in the scale of several orders of magnitude, upon UV irradiation, showing that fast in situ curing occurs enabling retention of the extruded shapes. FTIR analysis demonstrated that the degree of curing initially increased rapidly, then reached a plateau due to the inhibition of produced long chain

on monomer movement. The curing depth data indicated that a penetration depth equal to the filament diameter was reached after only a few seconds of irradiation. Samples with self-supported and complex shapes were successfully printed, indicating that the approach provides an excellent capability of shape retention of structures with suspended features. Pyrolysis led to the production of SiOC samples, including sandwich panels with a truss core, with limited deformation and no defects. Four-point bending test on the sandwich panels showed that they possessed a characteristic failure load of 38.8 N, with a narrow Weibull distribution with *m* of 6.1, demonstrating their potential as lightweight structural components for applications at high temperature or in harsh environments.

CRediT authorship contribution statement

Kai Huang: Writing – review & editing, Writing – original draft, Visualization, Methodology, Investigation, Formal analysis, Data curation, Funding acquisition. **Anna De Marzi**: Writing – review & editing, Investigation, Formal analysis, Data curation, Visualization. **Giorgia Franchin**: Writing – review & editing, Visualization, Conceptualization, Formal analysis. **Paolo Colombo**: Writing – review & editing, Visualization, Validation, Supervision, Methodology, Conceptualization

Conflicts of interest

There are no conflicts to declare.

Acknowledgements

K.H gratefully acknowledges the support of the China Scholarship Council (CSC) (No. 201804910741). The contribution of Michele Vibrante and Alessia Arbisan to the experiments is gratefully acknowledged. This study was carried out within the MICS (Made in Italy – Circular and Sustainable) Extended Partnership and received funding from the European Union Next-GenerationEU (PIANO NAZIONALE DI RIPRESA E RESILIENZA (PNRR) – MISSIONE 4 COMPONENTE 2, INVESTIMENTO 1.3–D.D.1551.11–10-2022, PE00000004). This manuscript reflects only the authors' views and opinions, neither the European Union nor the European Commission can be considered responsible for them.

Reference

[1] Y. Lakhdar, C. Tuck, J. Binner, A. Terry, R. Goodridge, Additive manufacturing of advanced ceramic materials, Progress in Materials Science 116 (2021) 100736.

[2] A. Zocca, P. Colombo, C.M. Gomes, J. Günster, Additive manufacturing of ceramics: issues, potentialities, and opportunities, J Am Ceram Soc 98(7) (2015) 1983-2001.

[3] T. Moritz, S. Maleksaeedi, Additive manufacturing of ceramic components, Additive Manufacturing, Elsevier2018, pp. 105-161.

[4] J.-C. Wang, H. Dommati, S.-J. Hsieh, Review of additive manufacturing methods for high-performance ceramic materials, The International Journal of Advanced Manufacturing Technology 103(5) (2019) 2627-2647.

[5] E. Feilden, D. Glymond, E. Saiz, L. Vandeperre, High temperature strength of an ultra high temperature ceramic produced by additive manufacturing, Ceramics International 45(15) (2019) 18210-18214.

[6] Z.C. Eckel, C. Zhou, J.H. Martin, A.J. Jacobsen, W.B. Carter, T.A. Schaedler, Additive manufacturing of polymer-derived ceramics, Science 351(6268) (2016) 58-62.

[7] J. Kelly, L. Finkenauer, P. Roy, J. Stolaroff, D. Nguyen, M. Ross, A. Hoff, J. Haslam, Binder Jet Additive Manufacturing of Ceramic Heat Exchangers for Concentrating Solar Power Applications with Thermal Energy Storage in Molten Chlorides, Additive Manufacturing (2022) 102937.

[8] C.L. Cramer, E. Ionescu, M. Graczyk-Zajac, A.T. Nelson, Y. Katoh, J.J. Haslam, L. Wondraczek, T.G. Aguirre, S. LeBlanc, H. Wang, Additive manufacturing of ceramic materials for energy applications: Road map and opportunities, Journal of the European Ceramic Society (2022).

[9] L. Tabard, E. Prud'Homme, V. Garnier, L. Gremillard, Hierarchical salt-ceramic composites for efficient thermochemical energy storage, Applied Materials Today 20 (2020) 100658.

[10] S.B. Mujib, R. Cuccato, S. Mukherjee, G. Franchin, P. Colombo, G. Singh, Electrospun SiOC ceramic fiber mats as freestanding electrodes for electrochemical energy storage applications, Ceramics International 46(3) (2020) 3565-3573.

[11] H.A. Colorado, E.I.G. Velásquez, S.N. Monteiro, Sustainability of additive manufacturing: the circular economy of materials and environmental perspectives, Journal of Materials Research and Technology 9(4) (2020) 8221-8234.

[12] R. König, M. Spaggiari, O. Santoliquido, P. Principi, G. Bianchi, A. Ortona, Micropollutant adsorption from water with engineered porous ceramic architectures produced by additive manufacturing and coated with natural zeolite, Journal of Cleaner Production 258 (2020) 120500.

[13] Z. He, T. Shanmugasundaram, G. Singh, Inkjet 3D printing of clay ceramics for water treatment, Progress in Additive Manufacturing 3(4) (2018) 215-219.

[14] Z. Chen, D. Zhang, E. Peng, J. Ding, 3D-printed ceramic structures with in situ grown whiskers for effective oil/water separation, Chemical Engineering Journal 373 (2019) 1223-1232.
[15] C. Jiao, D. Xie, Z. He, H. Liang, L. Shen, Y. Yang, Z. Tian, G. Wu, C. Wang, Additive manufacturing of Bio-inspired ceramic bone Scaffolds: Structural Design, mechanical properties and biocompatibility, Materials & Design 217 (2022) 110610.
[16] K. Sakthiabirami, J.-H. Kang, J.-G. Jang, V. Soundharrajan, H.-P. Lim, K.-D. Yun, C. Park, B.-N. Lee, Y.P. Yang, S.-W. Park, Hybrid porous zirconia scaffolds fabricated using additive manufacturing for bone tissue engineering applications, Materials Science and Engineering: C 123 (2021) 111950.
[17] S. Esslinger, R. Gadow, Additive manufacturing of bioceramic scaffolds by combination of FDM and slip casting, Journal of the European Ceramic Society 40(11) (2020) 3707-3713.
[18] H. Elsayed, C. Gardin, L. Ferroni, B. Zavan, P. Colombo, E. Bernardo, Highly Porous Sr/Mg‐Doped Hardystonite Bioceramics from Preceramic Polymers and Reactive Fillers: Direct Foaming and Direct Ink Writing, Adv Eng Mater 21(6) (2019) 1800900.
[19] X. Zhang, K. Zhang, L. Zhang, W. Wang, Y. Li, R. He, Additive manufacturing of cellular ceramic structures: from structure to structure-function integration, Materials & Design (2022) 110470.
[20] T.D. Ngo, A. Kashani, G. Imbalzano, K.T. Nguyen, D. Hui, Additive manufacturing (3D printing): A review of materials, methods, applications and challenges, Composites Part B: Engineering 143 (2018) 172-196.
[21] W. Gao, Y. Zhang, D. Ramanujan, K. Ramani, Y. Chen, C.B. Williams, C.C. Wang, Y.C. Shin, S. Zhang, P.D. Zavattieri, The status, challenges, and future of additive manufacturing in engineering, Computer-Aided Design 69 (2015) 65-89.
[22] S.A. Tofail, E.P. Koumoulos, A. Bandyopadhyay, S. Bose, L. O'Donoghue, C. Charitidis, Additive manufacturing: scientific and technological challenges, market uptake and opportunities, Materials today 21(1) (2018) 22-37.
[23] J.A. Lewis, J.E. Smay, J. Stuecker, J. Cesarano, Direct ink writing of three‐dimensional ceramic structures, J Am Ceram Soc 89(12) (2006) 3599-3609.
[24] S. Tang, L. Yang, X. Liu, G. Li, W. Jiang, Z. Fan, Direct ink writing additive manufacturing of porous alumina-based ceramic cores modified with nanosized MgO, Journal of the European Ceramic Society 40(15) (2020) 5758-5766.
[25] C.M. Larson, J.J. Choi, P.A. Gallardo, S.W. Henderson, M.D. Niemack, G. Rajagopalan, R.F. Shepherd, Direct ink writing of silicon carbide for microwave optics, Adv Eng Mater 18(1) (2016) 39-45.
[26] Z. Zhao, G. Zhou, Z. Yang, X. Cao, D. Jia, Y. Zhou, Direct ink writing of continuous SiO2 fiber reinforced wave-transparent ceramics, Journal of Advanced Ceramics 9(4) (2020) 403-412.

[27] R. Wang, P. Zhu, W. Yang, S. Gao, B. Li, Q. Li, Direct-writing of 3D periodic TiO2 bio-ceramic scaffolds with a sol-gel ink for in vitro cell growth, Materials & Design 144 (2018) 304-309.
[28] Q. Jiang, D. Yang, H. Yuan, R. Wang, M. Hao, W. Ren, G. Shao, H. Wang, J. Cui, J. Hu, Fabrication and properties of Si2N2O-Si3N4 ceramics via direct ink writing and low-temperature sintering, Ceramics International 48(1) (2022) 32-41.
[29] G. Franchin, H. Elsayed, R. Botti, K. Huang, J. Schmidt, G. Giometti, A. Zanini, A. De Marzi, M. D'Agostini, P. Scanferla, Y. Feng, P. Colombo, Additive Manufacturing of Ceramics from Liquid Feedstocks, Chinese Journal of Mechanical Engineering: Additive Manufacturing Frontiers 1(1) (2022) 100012.
[30] T. Bhattacharjee, S.M. Zehnder, K.G. Rowe, S. Jain, R.M. Nixon, W.G. Sawyer, T.E. Angelini, Writing in the granular gel medium, Sci Adv 1(8) (2015) e1500655.
[31] Y. Kim, H. Yuk, R. Zhao, S.A. Chester, X. Zhao, Printing ferromagnetic domains for untethered fast-transforming soft materials, Nature 558(7709) (2018) 274-279.
[32] D. Kokkinis, M. Schaffner, A.R. Studart, Multimaterial magnetically assisted 3D printing of composite materials, Nat Commun 6 (2015) 8643.
[33] J. Plog, Y. Jiang, Y. Pan, A.L. Yarin, Electrostatically-assisted direct ink writing for additive manufacturing, Additive Manufacturing 39 (2021) 101644.
[34] L. Friedrich, R. Collino, T. Ray, M. Begley, Scaling Relationships for Direct Ink Writing with Acoustic Focusing, TMS 2017 146th Annual Meeting & Exhibition Supplemental Proceedings, Springer, 2017, pp. 137-145.
[35] L. Friedrich, R. Collino, T. Ray, M. Begley, Acoustic control of microstructures during direct ink writing of two-phase materials, Sensors and Actuators A: Physical 268 (2017) 213-221.
[36] R.R. Collino, T.R. Ray, R.C. Fleming, J.D. Cornell, B.G. Compton, M.R. Begley, Deposition of ordered two-phase materials using microfluidic print nozzles with acoustic focusing, Extreme Mechanics Letters 8 (2016) 96-106.
[37] J.E. Aw, X. Zhang, A.Z. Nelson, L.M. Dean, M. Yourdkhani, R.H. Ewoldt, P.H. Geubelle, N.R. Sottos, Self‐Regulative Direct Ink Writing of Frontally Polymerizing Thermoset Polymers, Advanced Materials Technologies (2022) 2200230.
[38] I.D. Robertson, H.L. Hernandez, S.R. White, J.S. Moore, Rapid stiffening of a microfluidic endoskeleton via frontal polymerization, ACS Appl Mater Interfaces 6(21) (2014) 18469-74.
[39] I.D. Robertson, M. Yourdkhani, P.J. Centellas, J.E. Aw, D.G. Ivanoff, E. Goli, E.M. Lloyd, L.M. Dean, N.R. Sottos, P.H. Geubelle, J.S. Moore, S.R. White, Rapid energy-efficient manufacturing of polymers and composites via frontal polymerization, Nature 557(7704) (2018) 223-227.
[40] D.A. Rau, J. Herzberger, T.E. Long, C.B. Williams, Ultraviolet-assisted direct ink write to additively manufacture all-aromatic polyimides, ACS applied

materials & interfaces 10(41) (2018) 34828-34833.
[41] K. Chen, X. Kuang, V. Li, G. Kang, H.J. Qi, Fabrication of tough epoxy with shape memory effects by UV-assisted direct-ink write printing, Soft Matter 14(10) (2018) 1879-1886.
[42] Y. Guo, J. Xu, C. Yan, Y. Chen, X. Zhang, X. Jia, Y. Liu, X. Wang, F. Zhou, Direct ink writing of high performance architectured polyimides with low dimensional shrinkage, Adv Eng Mater 21(5) (2019) 1801314.
[43] H. Wang, C. Chen, F. Yang, Y. Shao, Z. Guo, Direct ink writing of metal parts with curing by UV light irradiation, Materials Today Communications 26 (2021) 102037.
[44] A. De Marzi, G. Giometti, J. Erler, P. Colombo, G. Franchin, Hybrid additive manufacturing for the fabrication of freeform transparent silica glass components, Additive Manufacturing 54 (2022) 102727.
[45] J. Chen, H. Ji, J. Zhang, S. Wang, Y. Liu, Fabrication of YAG ceramic tube by UV-assisted direct ink writing, Ceramics International 48(14) (2022) 19703-19708.
[46] Y. de Hazan, M. Thänert, M. Trunec, J. Misak, Robotic deposition of 3d nanocomposite and ceramic fiber architectures via UV curable colloidal inks, Journal of the European Ceramic Society 32(6) (2012) 1187-1198.
[47] K. Chen, L. Zhang, X. Kuang, V. Li, M. Lei, G. Kang, Z.L. Wang, H.J. Qi, Dynamic Photomask-Assisted Direct Ink Writing Multimaterial for Multilevel Triboelectric Nanogenerator, Adv Funct Mater 29(33) (2019) 1903568.
[48] W.-Y. Maeng, J.-W. Jeon, J.-B. Lee, H. Lee, Y.-H. Koh, H.-E. Kim, Photocurable ceramic/monomer feedstocks containing terpene crystals as sublimable porogen for UV curing-assisted 3D plotting, Journal of the European Ceramic Society (2020).
[49] L. Wei, J. Li, S. Zhang, B. Li, Y. Liu, F. Wang, S. Dong, Fabrication of SiOC ceramic with cellular structure via UV-Assisted direct ink writing, Ceramics International (2019).
[50] H. Dong, B. Hu, W. Zhang, W. Xie, J. Mo, H. Sun, J. Shang, Robotic-assisted automated in situ bioprinting, International Journal of Bioprinting 9(1) (2023).
[51] M.A. Skylar-Scott, S. Gunasekaran, J.A. Lewis, Laser-assisted direct ink writing of planar and 3D metal architectures, P Natl Acad Sci USA 113(22) (2016) 6137-6142.
[52] A. De Marzi, M. Vibrante, M. Bottin, G. Franchin, Development of robot assisted hybrid additive manufacturing technology for the freeform fabrication of lattice structures, Additive Manufacturing 66 (2023) 103456.
[53] G. Das, G. Mariotto, A. Quaranta, Microstructural evolution of thermally treated low-dielectric constant SiOC: H films prepared by PECVD, Journal of the Electrochemical Society 153(3) (2006) F46.
[54] Y. Bolbukh, K. Terpiłowski, R. Kozakevych, D. Sternik, A. Deryło-Marczewska, V. Tertykh, Modified silicas with different structure of grafted methylphenylsiloxane layer, Nanoscale Research Letters 11(1) (2016) 1-15.

[55] P.J. Launer, B. Arkles, Infrared analysis of organosilicon compounds: spectra-structure correlations, Silicone compounds register and review 100 (1987).
[56] K. Wu, J. Halloran, Photopolymerization monitoring of ceramic stereolithography resins by FTIR methods, Journal of Materials Science 40(1) (2005) 71-76.
[57] F. Jiang, D. Drummer, Curing kinetic analysis of acrylate photopolymer for additive manufacturing by photo-DSC, Polymers 12(5) (2020) 1080.
[58] F. Jiang, A. Wörz, M. Romeis, D. Drummer, Analysis of UV-Assisted direct ink writing rheological properties and curing degree, Polymer Testing 105 (2022) 107428.
[59] P. Jacobs, Rapid Prototyping & Manufacturing: Fundamentals of Stereolithography (Dearborn, MI: Society of Manufacturing Engineers) p 434 Go to reference in article, (1992).
[60] P. Jacobs, Stereolithography and Other RP&M Technologies. Society of Manufacturing Engineers, New York (1996) 1-26.
[61] P.F. Jacobs, Rapid prototyping & manufacturing: fundamentals of stereolithography, Society of Manufacturing Engineers1992.
[62] W. Weibull, A statistical distribution function of wide applicability, Journal of applied mechanics (1951).
[63] S.A. Rodrigues, Jr., J.L. Ferracane, A. Della Bona, Flexural strength and Weibull analysis of a microhybrid and a nanofill composite evaluated by 3- and 4-point bending tests, Dent Mater 24(3) (2008) 426-31.
[64] P. O'Connor, A. Kleyner, Practical reliability engineering, John Wiley & Sons2012.
[65] R. Morrell, Flexural strength testing of ceramics and hardmetals, (2007).
[66] A. Bernard, E. Bos-Levenbach, The plotting of observations on probability-paper, Stichting Mathematisch Centrum. Statistische Afdeling (SP 30a/55) (1955).
[67] B. Demchyna, T. Osadchuk, Flexural strength of glass using Weibull statistic analysis, Journal of Achievements in Materials and Manufacturing Engineering 87(2) (2018) 49-61.
[68] A. Fernandez, M. Vázquez, Improved estimation of weibull parameters considering unreliability uncertainties, IEEE Transactions on Reliability 61(1) (2011) 32-40.
[69] U. Genschel, W.Q. Meeker, A comparison of maximum likelihood and median-rank regression for Weibull estimation, Quality engineering 22(4) (2010) 236-255.

Table of content